Extraction and Quantification of Left Ventricular Deformation Modes

Espen W. Remme*, Alistair A. Young, Kevin F. Augenstein, Brett Cowan, and Peter J. Hunter

***Abstract*—We have developed a method that decomposes the deformation of the left ventricle (LV) between end diastole (ED) and end systole (ES) into separate deformation modes such as longitudinal shortening, wall thickening, and twisting. The deformation was initially found from the motion of an LV finite-element mesh that was fitted to clinically obtained magnetic resonance (MR) tagged images. A mode coefficient was calculated for each deformation mode to quantify the different modes and, thus allowing for discrimination of normal and abnormal deformation patterns. We applied the method to 13 normal subjects and 13 diabetes patients. By using the ED mesh as reference and adding the extracted deformation modes multiplied by their mode coefficients, an approximate ES mesh was calculated and compared with the "true" ES mesh found from the MR images. For the 26 subjects the average Euclidean distance was less than 1.7 ± 0.9 mm between the nodes of the approximated and true ES meshes. The coefficient values for the patient group showed significantly less longitudinal shortening, less wall thickening, more longitudinal twisting and also more bulging of the septum into the LV when compared with the normal subjects. We conclude that the developed method successfully quantifies the deformation into several modes of deformation and is capable of distinguishing the deformation of a group of patients from a group of normal subjects.**

***Index Terms*—Finite-element model, left ventricular deformation modes, MRI tagging.**

I. Introduction

THE deformation of the left ventricular (LV) wall during the heart cycle is affected via the material properties by cardiac diseases. Some heart conditions may be identified by the specific influence they have on the deformation. A method that decomposes and quantifies the deformation of the LV into separate modes, such as longitudinal shortening, wall-thickening, and base-apex twist, between end diastole (ED) and end systole (ES) is required in order to characterize deformation patterns and separate diseased hearts from normal hearts. It could be used to examine the severity of the disease and ultimately it may be possible to automatically identify the type of disease by comparing a subject's deformation modes with a database of modes from different cases.

Such a method for quantifying the different types of deformation mode may also be helpful in mathematical modeling and simulations of the heart cycle. By changing the material or other biophysical parameters in the model we can use the deformation modes to gain an understanding of the function and effect of the various model parameters on the myocardial deformation and performance.

Previously, Arts *et al.* [1] used an ellipsoidal model as an approximation to the LV. The ellipsoid was deformed according to specified deformation modes such as cavity volume change, torsion, and elliptification. The amount of deformation caused by each mode was controlled by its mode coefficient. The mode coefficients were calculated by fitting their resulting deformation to measured displacements of implanted markers. Park *et al.* [2] developed a generalized elliptical model of the LV where the model geometry was described by a set of parameters. These parameters were functions of position and time and the different parameters controlled different types of deformation. The parameter values were fitted to the motion obtained from magnetic resonance tagged data, providing a means to quantify the LV deformation into different deformation modes. O'Dell *et al.* [3] reported deformation modes based on the prolate spheriodal coordinate system. However, none of these studies attempted to characterize deformation modes in terms of normal and disease populations.

Magnetic resonance imaging (MRI) tissue tagging [4], [5] can be coupled with finite-element (FE) modeling to provide a noninvasive method for quantifying LV motion with an advanced geometric model [6], [7]. The aim of our study was to develop a method based on an FE model of the LV myocardium to decompose and quantify the deformation of the model between ED and ES into specific deformation modes. We wanted to find modes with a clear clinical interpretation, that are relatively independent of one another and which sum together to accurately capture the total deformation. The developed method was evaluated on a group of normal subjects and a group of patients with diffuse cardiac function abnormalities due to type-2 diabetes mellitus in order to investigate the method's ability to distinguish between healthy and diseased cardiac deformation patterns.

II. Methods

A. Subjects

Anatomical and tagged MR images were acquired in 13 normal volunteers (age 23 ± 3 years, four female, 70 ± 15 kg,

Manuscript received November 24, 2003; revised March 21, 2004. This work was supported in part by the Research Council of Norway under Grant 128267/320 and Grant 139327/300. *Asterisk indicates corresponding author.*

*E. W. Remme was with the Bioengineering Institute, University of Auckland, New Zealand on leave from the the Department of Circulation and Medical Imaging, Norwegian University of Science and Technology, Trondheim, Norway. He is now with the Institute for Surgical Research, Rikshospitalet University Hospital, Oslo, Norway (e-mail: espen.remme@medisin.uio.no).

A. A. Young is with the Department of Anatomy with Radiology, University of Auckland, Auckland 00, New Zealand (e-mail: a.young@auckland.ac.nz).

K. F. Augenstein and P. J. Hunter are with the Bioengineering Institute, University of Auckland, Auckland 00, New Zealand (e-mail: k.augenstein@auckland.ac.nz; p.hunter@auckland.ac.nz).

B. Cowan is with the Department of Medicine, University of Auckland, Auckland 00, New Zealand (e-mail: b.cowan@auckland.ac.nz).

Digital Object Identifier 10.1109/TBME.2004.834283

116±15 mmHg systolic blood pressure) who had no history of cardiac disease. The same imaging procedure was applied to a group of 13 patients with type 2 diabetes mellitus (age 49±7 years, 5 female, 96±26 kg, 135±13 mmHg systolic blood pressure). All patients had evidence of diastolic dysfunction by echocardiography (either abnormal or pseudonormal filling pattern) but none had evidence of coronary artery disease or localized regional wall motion abnormalities. All patients had apparently normal systolic function by standard echocardiographic examination (fractional shortening within normal bounds and no evidence of regional wall motion abnormalities). These patients are thought to suffer from a diabetic cardiomyopathy, found in approximately 30% of patients with type-2 diabetes and characterized by abnormal myocardial relaxation and elevated LV filling pressures. Histologically, these patients have interstitial fibrosis with increased amounts of collagen, glycoprotein, triglycerides, and cholesterol in the myocardial interstitium, and in some cases intimal thickening, hyaline deposition, and inflammatory changes have been observed in small intramural arteries [8].

B. Imaging

All imaging was performed on a 1.5 T Siemens Vision magnet with a phased array body coil. Prospectively gated untagged, anatomical cardiac cine images were acquired in 8–9 short-axis slices and 3 long-axis slices using a segmented k-space pulse sequence ($\mathrm{TE/TR} = 4.8/9.9$ msec, flip angle $= 15°$, FOV 280–350 mm, 7 or 9 views per segment, 128 × 256 image matrix) with view-sharing (giving 11–19 frames per slice). Each slice was acquired during a breath hold of 15–19 cardiac cycles at end-tidal lung volume. The short-axis slices spanned the heart from apex to base with a slice thickness of 8.0 mm and interslice gap of 0.0–3.0 mm. The long-axis image slices were acquired at equal 60° increments around the LV central axis, starting at the plane passing through the mid-septum, center of the LV cavity and LV free-wall.

Short-axis tagged images of the heart were acquired at the same positions as the cine untagged, anatomical images using a prospectively gated, view-shared, breath-hold, segmented k-space version of the SPAMM imaging sequence [9]. The tag spacing in the orthogonal grid pattern was 8 mm and the tag lines were oriented at 45° relative to the imaging axes. The imaging parameters were the same as those used for the breath-hold cine MRI acquisition described above, except for $\mathrm{TE/TR} = 4.0/8.9$ msec. A set of six long-axis tagged image slices was also acquired at equal 30° increments around the LV central axis.

C. Finite-Element (FE) Model Construction

For each subject the LV endocardial and epicardial surfaces were manually segmented in the untagged, anatomical images for the frame corresponding to ES. An FE mesh was fitted to the segmented geometry by minimizing (in a least-squares sense) the distance between the segmented surface points and the surfaces of the FE mesh [10], [11]. A 16-element FE model was created in rectangular Cartesian coordinates consisting of 4 circumferential, 4 longitudinal, and 1 transmural elements. The geometric interpolation functions were cubic Hermite in the circumferential (ξ_1) and longitudinal (ξ_2) directions (for C^1 continuity) and linear in the transmural (ξ_3) direction. The interpolation is given by $u(\xi_1,\xi_2,\xi_3) = \sum_{k=1}^{K} \Psi_k(\xi_1,\xi_2,\xi_3)u_k$, where Ψ_k are the tensor product element basis functions and u represents the interpolated scalar function (e.g., x, y,or z coordinate) inside the element. The bicubic-linear interpolation results in 4 parameters per field per node of the model. These parameters directly define the value of the field (u), the first derivatives $\partial \mathrm{u}/\partial\xi_1$ and $\partial \mathrm{u}/\partial\xi_2$, and the cross derivative $\partial^2 \mathrm{u}/(\partial\xi_1\partial\xi_2)$ at each node.

A standard FE mesh structure and orientation was applied to each heart. The LV long-axis was aligned with the x-axis and the middle of the right ventricle with the y-axis. The longitudinal node positions were spaced equally from apex to base. In this manner, we could treat the nodes as homologous (i.e., matching) points between subjects.

D. Estimation of LV Deformation From MRI Tags

Tag stripes were located and tracked in the MR tagged images using a semi-automated tracking procedure, based on an active contour grid model, which has been previously described and validated [6], [7]. This enabled tag stripes to be tracked in each slice to determine the exact position and motion of several hundred points in the myocardium.

The three-dimensional motion best fitting the tracked image tag points was reconstructed with the aid of the FE model, as described previously [7]. Since the myocardium moves through the imaging plane from frame to frame, material points within the LV are generally imaged only once in the cine time sequence. Thus, the tracked image stripe points do not correspond to the same set of material points in the heart. However, initially (in frame 1 shortly after tag creation) the tags are straight and orthogonal to the image planes. Each stripe point in each subsequent frame, therefore, provides a one-dimensional constraint on the displacement back to the initial frame: the displacement orthogonal to the original tag plane is known but the displacements parallel to the tag plane are not. In the present application, the location of all the tracked stripe points at ES were determined within the ES model (fitted to the segmented boundaries at ES as described above). This allowed calculation of the model (material) coordinates $\boldsymbol{\xi}_\mathrm{d}$ of each datapoint d within the ES model. The nodal parameters of the FE mesh at ED were then found by minimizing the following objective function with respect to the nodal mesh parameters:

$$E(\mathbf{x}) = S(\mathbf{x}) + \sum_d \left[\mathbf{n}_d \cdot (\mathbf{x}(\boldsymbol{\xi}_d) - \mathbf{x}_d)\right]^2. \tag{1}$$

The smoothing constraint $\mathrm{S}(\mathbf{x})$ is included to regularize the problem in case of nonuniformly distributed data. The tag points, $\mathbf{x}_\mathrm{d}$, are points along the lines where the tag-planes intersect the images at ED. Each point has coordinates $\mathbf{x}_\mathrm{d}$ and a normal vector $\mathbf{n}_\mathrm{d}$ (in practice the normal to the corresponding tag-plane at ED). The location of the FE model point corresponding to $\mathbf{x}_\mathrm{d}$ is given as $\mathbf{x}(\boldsymbol{\xi}_\mathrm{d})$ where $\boldsymbol{\xi} = (\xi_1,\xi_2,\xi_3)$ are the model's material coordinates. Thus, only the component along the tag-plane normal is penalized in the error term in (1).

The ES mesh and the ED mesh found from the MRI data are referred to in the following as the "true" meshes.

After the tag fitting any rigid body motion was removed between the ED and ES meshes by translating and rotating these meshes so that their epicardial apex nodes were at the same point on the x axis, their long-axis (from apex to the center of gravity of the base nodes) was aligned with the x axis, and the node corresponding to the middle of the septum was rotated to lie on the y axis.

There was an order of magnitude or more difference between the field value, u, (where u is the x, y, or z coordinate) and its derivatives $\partial \mathrm{u}/\partial\xi_1$, $\partial \mathrm{u}/\partial\xi_2$, and $\partial^2 \mathrm{u}/(\partial\xi_1\partial\xi_2)$. This potential scaling problem was eliminated by subdividing the mesh in the circumferential and longitudinal directions, giving a mesh structure of 12 circumferential and 12 longitudinal elements and a total of 290 nodes. Discarding the nodal derivative information, only the nodal x, y, and z coordinates were used in the rest of the mode analysis.

E. Mode Decomposition

To guide the selection of the modes, we performed a principal component analysis (PCA) on the deformation as previously described in [12]. The principle of the method was to separate the deformation into independent modes by forming a matrix of deformations from several subjects and extracting the eigenvectors and eigenvalues. The x, y, and z coordinates at each of the $\mathrm{N} = 290$ nodes of the subdivided ED mesh were entered in a column vector: $\mathbf{x}_{\mathrm{ED}} = [\mathrm{x}_1, \mathrm{y}_1, \mathrm{z}_1, \ldots, \mathrm{z}_{\mathrm{N}}]^{\mathrm{T}}$, where $^{\mathrm{T}}$ is the transpose operator. A similar vector was constructed for the ES mesh: $\mathbf{x}_{\mathrm{ES}}$. The displacement vector was calculated as the difference between the two: $\mathbf{d} = \mathbf{x}_{\mathrm{ES}} - \mathbf{x}_{\mathrm{ED}}$. The mean displacement vector was found for all $\mathrm{S} = 26$ subjects (normals + patients) as $\mathbf{d}_{\mathrm{m}} = 1/\mathrm{S} * \sum_{\mathrm{s}} \mathbf{d}_{\mathrm{s}}$, where $\mathbf{d}_{\mathrm{s}}$ is the displacement vector of subject s. The covariance matrix C was formed as shown in (2) where P is an orthogonal matrix, which contains the modes of the variation and Λ is a diagonal matrix of eigenvalues. Each column $\mathbf{P}_{\mathrm{i}}$ of P contains the mode associated with the corresponding diagonal element of Λ. Assuming the modes were normally distributed about zero, the variance of each mode was σ_{i}^2, the ith diagonal element of Λ

$$B = \begin{bmatrix} | & | & & | \\ \mathbf{d}_1 - \mathbf{d}_{\mathrm{m}} & \mathbf{d}_2 - \mathbf{d}_{\mathrm{m}} & \cdots & \mathbf{d}_S - \mathbf{d}_{\mathrm{m}} \\ | & | & & | \end{bmatrix}$$
$$C = \frac{1}{S} BB^T = P\Lambda P^T. \tag{2}$$

The PCA provided a tool to analyze the deformation modes that varied the most between subjects. To find out what these modes looked like we plotted the mean ES mesh for all subjects together with the two meshes obtained by adding $\pm 2\sigma_{\mathrm{i}} \cdot \mathbf{P}_{\mathrm{i}}$ to the mean displacement vector between ED and ES. This was done for the two most significant modes $\mathrm{i} = 1, 2$. A sketch of the results is shown in Fig. 1. Though the PCA gave orthogonal modes, the resulting modes were not intuitively understandable as they were a mixture of simple modes such as longitudinal shortening, wall thickening, twist, etc and they could also have regional variations. Thus, their physiological meanings were difficult to interpret, but the main features could still be found as shown in Fig. 1.

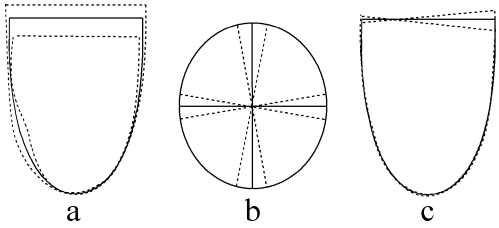

Fig. 1. The figure shows a schematic of the variance of the ES mesh after performing a PCA. The solid line represents the mean ES mesh while the dotted lines are the meshes obtained when adding $\pm 2\sigma_{\mathrm{i}} \cdot \mathbf{P}_{\mathrm{i}}$ to the mean deformation between ED and ES. That is, $\mathbf{x}_{\mathrm{ES}} = \mathbf{x}_{\mathrm{ED}}^{\mathrm{m}} + \mathbf{d}_{\mathrm{m}} \pm 2\sigma_{\mathrm{i}} \cdot \mathbf{P}_{\mathrm{i}}$ where $\mathbf{x}_{\mathrm{ED}}^{\mathrm{m}}$ is the mean mesh at ED. For the first mode a large variance of the base-apex movement was seen together with a septal bulging (septum to the left) as illustrated in a). The second mode showed a variation of the twist angle as illustrated in b) where the LV is viewed from the apex and also a tilting behavior of the base between the septum (left) and the LV free-wall (right) as illustrated in c).

Instead of using the PCA modes we wanted to develop a method that used only simple deformation modes that were physiologically easy to interpret. Before selecting the modes certain requirements were set up for the choice of modes: each mode should have a physically intuitive meaning; the number of modes should be as small as possible consistent with representing the total deformation to an accuracy compatible with the measurement error; the modes should be relatively independent of each other; the mode coefficients in a group of similar subject should have low variances; the mode coefficients should be sensitive to disease states. Based on these requirements and the findings from the PCA, we selected the following modes (termed "clinical modes"): 1) longitudinal shortening, 2) wall-thickening, 3) "hinging" (where the apex serves as a hinge), 4–6) longitudinal twisting modes which included both circumferential-longitudinal shear and circumferential-radial shear, 7) longitudinal-radial (LR) shearing, 8) asymmetric base-apex shortening, 9) septal bulging.

To extract the specific modes the nodal coordinates were first converted from rectangular Cartesian (RC) coordinates to prolate spheroidal (PS) coordinates, see (3), as the PS coordinate axes were aligned in the circumferential (θ), longitudinal (μ), and radial (λ) directions of the LV. The PS coordinates, thus, provided an easy mechanism for changing the nodes positions in one of the respective heart coordinate directions: Changing the μ-coordinates of the nodes changed the base-apex length of the mesh, changing the λ-coordinate changed wall-thickness/transmural position of the wall, and changing the θ-coordinate created a twisting/rotation mode of the mesh. The focus, f, of the PS coordinate system was calculated by looking at the node corresponding to the epicardial free-wall at equator where $\mu = 90^\circ$ and $\theta = 180^\circ$. λ was set to 1. The focus was then calculated by rearranging (3b). It was calculated individually for each subject and, thus, provided a mechanism for normalizing between subjects with different sized hearts. After the mode had been created by changing the mesh's PS coordinates, the new node coordinates were converted back to RC coordinates

$$\begin{aligned} x &= f \cdot \cosh(\lambda)\cos(\mu) \\ y &= f \cdot \sinh(\lambda)\sin(\mu)\cos(\theta) \\ z &= f \cdot \sinh(\lambda)\sin(\mu)\sin(\theta). \end{aligned} \tag{3}$$

By using the ED mesh as starting mesh for extraction of each mode, the nodes of the ED mesh were changed accordingly. The longitudinal shortening mode was created by decreasing the μ-coordinate of the ED mesh base nodes by $\Delta\mu = -15^\circ$. The $\Delta\mu$ increment of the other nodes further down toward the apex were decreased linearly as a function of their row number, where rows were considered to be circumferential rings of nodes at approximately the same longitudinal position. Row 1 was the row of nodes closest to the apex and row 12 was the base nodes $(\mathrm{r_{base}})$. $\Delta\mu$ for the nodes on row r was then calculated as follows: $\Delta\mu = -15^\circ * \mathrm{r}/\mathrm{r_{base}}$. A feature of the PS coordinates is that a change of the nodal μ value while keeping λ and θ fixed would move the node along elliptical lines. This resulted in the base nodes, which typically ranged from 115° to 135° at ED, not only moved downwards but also outwards as their μ value was decreased and, thus increasing the base area. This was the opposite of what was actually seen occurring at the base between ED and ES. This problem was solved by keeping the y and z values unchanged for the nodes with a μ value over 90° (i.e., the nodes above equator) as they were before converting them to PS coordinates. The change of the μ value for these nodes, thus, only changed the x coordinate, which resulted in a movement straight up and down. The nodes below equator were moved along elliptical lines, which corresponded well with what we observed. This mode and the other created modes can be seen in Fig. 2.

The second mode was wall thickening. The epicardial nodes were fixed while the endocardial nodes were changed by $\Delta\lambda = -0.08$. The third mode was a hinge mode where the cavity volume was increased by fixing the apex nodes and moving the higher nodes in by $\Delta\lambda = -0.10 * \mathrm{r}/\mathrm{r_{base}}$.

Modes 4–6 were twisting modes. Previous studies have found that the LV twists significantly around the long axis [6], [13] and that the endocardium seems to twist more than the epicardium [6]. For the first twist mode (mode 4), all the epicardial nodes were fixed whereas the endocardial base nodes were rotated around $\Delta\theta = -7^\circ$. The $\Delta\theta$ increment for the nodes closer to apex varied linearly with their row number: $\Delta\theta = -7^\circ * \mathrm{r}/\mathrm{r_{base}}$. For mode 5, the twisting was reversed where now the endocardial nodes closest to the apex were rotated by $\Delta\theta = 25^\circ$ and the increment varied linearly to 0 toward the base. For mode 6, the procedure was repeated for the epicardial nodes. The endocardial nodes were fixed while the epicardial nodes closest to apex were rotated $\Delta\theta = 15^\circ$ and the increment varied linearly to 0 toward the base. The separation of the longitudinal twisting into these 3 modes incorporated both circumferential-longitudinal shearing as well as circumferential-radial shearing. We did not create a mode where the epicardial base nodes were twisted, as the procedure for removing the rigid body modes involved rotating the epicardial base node that corresponded to the mid-septum to align with the y axis both for the ED and ES mesh and, thus removing the epicardial base rotation.

Mode 7 was an LR shearing mode where the μ-coordinate for the endocardial nodes were increased by $\Delta\mu = -4^\circ$ while the epicardial nodes were changed by $\Delta\mu = 4^\circ$. The $\Delta\mu$ decreased linearly toward the apex as described for mode 1.

From the PCA results we decided to implement two asymmetric modes. One was a difference in longitudinal shortening between the septum and the LV free-wall, which appeared as a tilting of the base [Fig. 1(c)]. Mode 8 was, thus, a change of the longitudinal shortening between the septum and LV free-wall. This mode was created in a similar manner to mode 1 but for this mode there was also a linear variation of $\Delta\mu$ in the circumferential direction were the nodes are organized in columns of approximately same θ values. The result was a mode where the base was lifted at the septum $(\Delta\mu = 2^\circ)$ and lowered at free-wall side $(\Delta\mu = -10^\circ)$. The $\Delta\mu$ for each column of nodes varied linearly to zero at the apex as before.

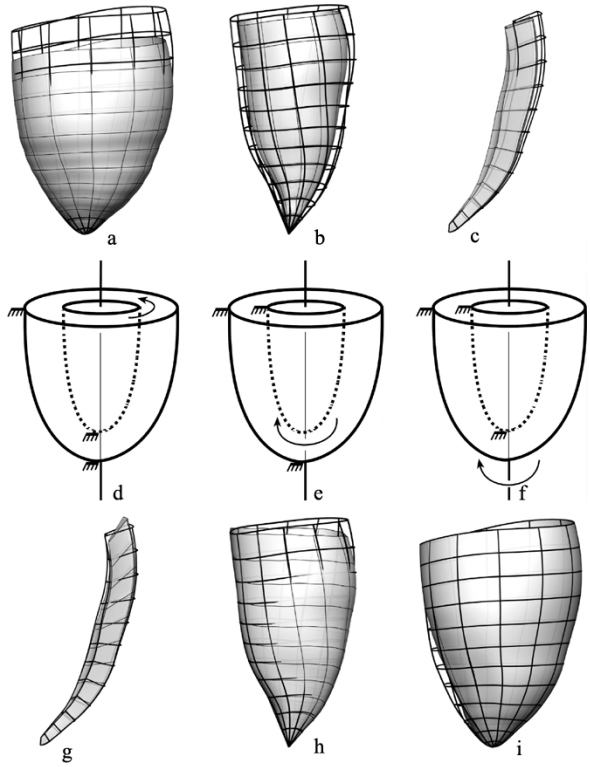

Fig. 2. The 9 created clinical modes of deformation. In (a)–(c) and (g)–(i) the thick lines correspond to the original ED mesh while the thin lines and shaded surfaces correspond to the mesh created for the respective deformation mode. (a) Longitudinal shortening mode, illustrated at the epicardial surface. (b) Wall thickening mode, the endocardial surface is moved inwards (the epicardial surface, not shown, is left unchanged). (c) Hinge mode, illustrated by a longitudinal slice of elements. (d) Twisting of the endocardial base, illustrated by a schematic of the LV where the endocardial surface is rotated at the base with gradually decreasing rotation toward apex while the epicardial surface is fixed. (e) Twisting of the endocardial apex. (f) Twisting of the epicardial apex. (g) Longitudinal-radial shearing, illustrated by a longitudinal slice of elements. (h) Tilting mode, illustrated at the endocardial surface. (i) Septal bulging, illustrated at the epicardial surface where the septum is to the left.

Mode 9 was a bulging of the septum into the LV. The mode was created by decreasing the λ value of the nodes in the specified area of the septum while all other nodes were fixed. $\Delta\lambda = -0.10$ was the peak value in the middle of the septum and varied linearly in a "circular fashion" to 0 at the apex and the row above equator as well as to 0 at the anterior and posterior sides.

F. Calculating the Coefficients

In a similar manner to the PCA the node coordinates were entered into column vectors $\mathbf{x}_{\mathrm{ED}}$ and $\mathbf{x}_{\mathrm{ES}}$ for the ED and ES mesh, respectively. Similarly, the coordinates of the created mesh for mode m were entered into vector $\mathbf{x}_{\mathrm{m}}$. The total deformation

could then be approximated by (4) where the mode coefficient, k_m, quantified mode m

$$\mathbf{x}_{ES} - \mathbf{x}_{ED} \approx \sum_m k_m(\mathbf{x}_m - \mathbf{x}_{ED}) \tag{4}$$

A least-squares calculation was used to calculate the coefficients, k_m, as shown in (5) where M is the number of modes. Note that this approach linearizes the deviations about a set of default deformations

$$D = \begin{bmatrix} | & | & & | \\ \mathbf{x}_1 - \mathbf{x}_{ED} & \mathbf{x}_2 - \mathbf{x}_{ED} & \cdots & \mathbf{x}_M - \mathbf{x}_{ED} \\ | & | & & | \end{bmatrix},$$

$$\mathbf{k} = \begin{bmatrix} k_1 \\ k_2 \\ \vdots \\ k_M \end{bmatrix}$$

$$\mathbf{k} = (D^T D)^{-1} D^T (\mathbf{x}_{ES} - \mathbf{x}_{ED}) \tag{5}$$

G. Validations

The method was applied to 13 normal subjects and 13 patients. Several tests were performed to validate the method:

An independence test of the modes was performed by extracting the correlations between the mode coefficients from the matrix $(D^T D)^{-1}$ that contained the variances and covariances of the calculated coefficients [14]. Another test to investigate the coupling between the modes was performed by increasing the magnitude of one mode by 10% and keeping the other magnitudes to their default values and then calculate the mode coefficients, e.g., for mode 1, $\Delta\mu$ was changed from $\Delta\mu = -15°$ to $\Delta\mu = -16.5°$. Ideally, the only coefficient that should change was the coefficient for which the magnitude was changed.

The goodness of the approximation of (4) to the total deformation was checked by comparing the true ES mesh with the estimated ES mesh obtained by rearranging (4) and using each subject's calculated coefficients. The average Euclidean distance between the nodes of the two meshes, as shown in (6), was used as a measure for the goodness of the approximation. In (6) N is the number of nodes, x_{tn} is the $x$coordinate at node n for the true mesh while x_{mn} is the equivalent for the mesh obtained from (4). The significance of each mode to the reduction of this error was investigated by leaving out one mode at the time, and then calculate the coefficients and the ES mesh using only the eight remaining modes

$$E = \frac{1}{N}\sum_{n=1}^{N} \sqrt{(x_{mn} - x_{tn})^2 + (y_{mn} - y_{tn})^2 + (z_{mn} - z_{tn})^2}. \tag{6}$$

The final validation was to compare the calculated coefficients from the group of normal subjects with the group of patients to see if the method was able to distinguish between them. For this purpose we used an unpaired t test to test for significant differences between each mode. The significance level of the t test was corrected in Bonferroni fashion to control for inflation of the type 1 error rate over the nine comparisons performed (i.e., the p values for each test were multiplied by 9 and then compared with the nominal significance level of 0.05).

H. PCA Modes

The principle component analysis gave a set of orthogonal (independent) deformation modes, which describe the deviation from the mean displacement vector $\mathbf{d}_m$ of all subjects. These deformation modes are given as the column vectors of the matrix P. The deformation of each subject can be approximated using these modes as shown in (7) where V_s is the volume of the LV mesh of subject s and S is the total number of subjects. Volume was used as a scaling factor to correct for differences in size between patients. The advantage with the PCA modes is that the modes are orthogonal and, thus, there is no coupling between the mode coefficients. However, a disadvantage of PCA is that the modes have an unclear physiological interpretation. The coefficients calculated in (7c) were compared between the normals and patients as described above. The approximation in (7d) was checked by comparing the calculated ES mesh obtained by rearranging (7d) with the true ES mesh

$$B = \begin{bmatrix} | & | & & | \\ \frac{\mathbf{d}_1 - \mathbf{d}_m}{V_1} & \frac{\mathbf{d}_2 - \mathbf{d}_m}{V_2} & \cdots & \frac{\mathbf{d}_S - \mathbf{d}_m}{V_S} \\ | & | & & | \end{bmatrix} \tag{7a}$$

$$C = \frac{1}{S} BB^T = P\Lambda P^T \tag{7b}$$

$$\mathbf{k}_s = P^T \frac{(\mathbf{d}_s - \mathbf{d}_m)}{V_s} \tag{7c}$$

$$\mathbf{x}_{ES} - \mathbf{x}_{ED} \approx \mathbf{d}_m + P\mathbf{k}_s V_s \tag{7d}$$

I. Comparing Wall Thickness

The average wall thickness of the ES meshes of the normal subjects and patient group was calculated to see if there was any significant difference between the two groups. The average Euclidean distance between the endocardial nodes and their corresponding epicardial nodes, which were aligned with the transmural direction of the heart coordinate system, was found for each mesh and averaged for the two groups.

III. Results

The mode coefficients were generally uncoupled with only a small degree of correlation between most of the modes. The highest degree of correlations were between the longitudinal shortening mode and the tilting mode (−0.74), the wall thickening mode and the hinge mode (−0.63) and the endocardial twist of the base and apex (0.61). Table I shows the average correlation matrix for the 13 normal subjects. These results imply that the particular subjects studied, most modes are independent, with some coupling between modes 1 and 8 (which both control longitudinal shortening), modes 2 and 3 (which control inward motion of the heart during systole), and modes 4 and 5 (which control rotation about the central axis).

The sensitivity of the calculated coefficient values was low to changes of the amplitude of other modes beside itself. The mode coefficient for the mode that had its amplitude increased by 10% had its corresponding coefficient value decreased by ∼9% while the other coefficient remained virtually unchanged (less than 0.7% change for 70 out of 72 cases, the two others had a change of 1% and 1.5%).

TABLE I
CORRELATION MATRIX. THE ELEMENTS IN THE TABLE ARE THE CORRELATIONS BETWEEN THE VARIOUS MODE COEFFICIENTS EXTRACTED FROM THE MATRIX $(D^T D)^{-1}$. NOTE THAT THE MATRIX IS SYMMETRIC AND ONLY THE VALUES ON THE DIAGONAL AND BELOW ARE SHOWN

	k_1	k_2	k_3	k_4	k_5	k_6	k_7	k_8	k_9
k_1	1.00								
k_2	0.04	1.00							
k_3	-0.16	-0.63	1.00						
k_4	0.01	-0.09	0.00	1.00					
k_5	0.00	-0.11	0.02	0.61	1.00				
k_6	0.00	0.04	-0.05	0.00	-0.00	1.00			
k_7	0.10	0.02	-0.07	0.01	0.00	0.01	1.00		
k_8	-0.74	-0.00	-0.00	-0.00	-0.00	-0.00	0.01	1.00	
k_9	0.01	-0.14	-0.13	-0.01	-0.02	-0.03	0.02	0.03	1.00

TABLE II
THE TABLE SHOWS THE MEAN ERROR IN MM FOR ALL THE NODES OF THE MESHES OF THE SUBJECTS IN THE NORMAL GROUP AND THE PATIENT GROUP WHEN ONE MODE IS REMOVED FROM THE CALCULATION AT THE TIME

Removed mode	1	2	3	4	5	6	7	8	9
Normals	4.2	1.9	2.3	1.7	1.9	2.3	1.6	1.7	1.7
Patients	3.1	1.9	2.3	1.8	2.1	2.9	1.8	1.9	1.8

The average Euclidean distance between the 290 nodes of the "true" ES mesh and the approximated ES mesh ranged from 1.4±0.7 mm to 1.8±1.2 mm (mean±SD) with a mean of 1.6±0.1 mm for the group of normals and from 1.2±0.6 mm to 2.3±1.1 mm with a mean of 1.8±0.4 mm for the patients. The average Euclidian distance for all the nodes in all 26 meshes was 1.7±0.9 mm. The increase of this error when one mode at the time was excluded was markedly highest for the longitudinal shortening mode where the error increased to 4.2 mm for the normals and 3.1 for the patients. The lowest error increase was for the exclusion of mode 4, 7, and 9 which all had less than 0.1 mm error increase for the both subject groups. Table II shows the error for the exclusion of one mode at the time.

The calculated average mode coefficients between the normal and patient group showed some distinct differences. Table III shows the mean coefficient values±SD for the two groups. Fig. 3 shows a plot of the spread of the patient-coefficients with the mean±SD indicated for the normal subjects. Compared with the normals the patients had significantly reduced base-apex movement ($p < 0.0002$), reduced wall-thickening ($p < 0.0005$), more twisting of the apex (mode 5: $p < 0.003$, mode 6: $p < 0.003$), and they had significantly more bulging of the septum into the LV ($p < 0.02$). There was no significant differences between the coefficients for the hinge mode, endocardial base twist mode, and LR-shearing mode. The tilting mode was close to being significantly different ($p = 0.067$).

The calculated coefficients for the PCA modes are shown in Fig. 4 where the coefficient variance has been normalized by dividing by the square root of the variance of each mode, i.e., $k_i/\sqrt{(\lambda_i)}$. There was a clear difference in coefficient values for

TABLE III
MEAN CALCULATED MODE COEFFICIENTS AND THEIR STANDARD DEVIATIONS FOR THE NORMAL SUBJECTS AND PATIENTS

	k_1	k_2	k_3	k_4	k_5	k_6	k_7	k_8	k_9
Normals	1.00	0.74	0.99	0.43	0.69	0.86	0.12	0.17	-0.36
±SD	0.12	0.13	0.12	0.20	0.12	0.24	0.16	0.22	0.21
Patients	0.65	0.49	0.90	0.29	0.92	1.29	0.24	0.46	0.13
±SD	0.20	0.13	0.31	0.20	0.14	0.28	0.14	0.29	0.43

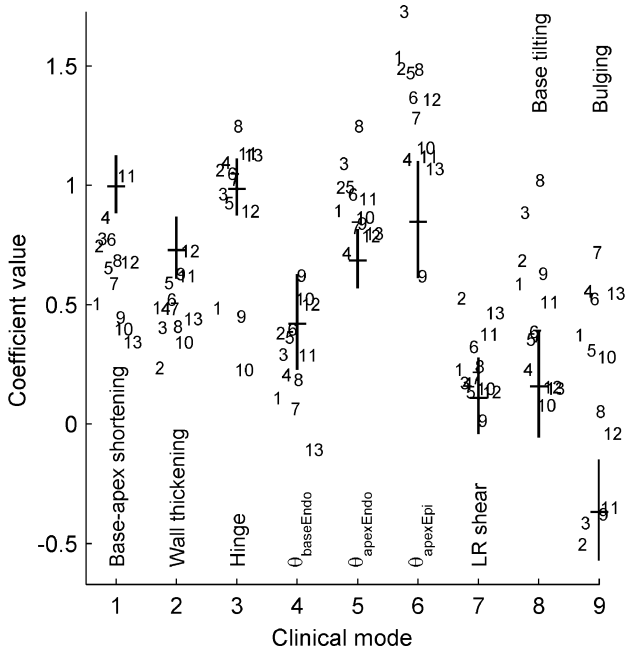

Fig. 3. The figure shows the mean coefficient value for the different clinical modes for the normal subjects marked with a short horizontal bar while the vertical line shows the ±SD variation. The coefficients for the patients are indicated with a number for each patient. Their horizontal spread from the mode line is included to separate better between the subjects.

the first mode between the normals and patients. None of the other mode coefficients were significantly different. The mean Eucledian distance between the true and approximated ES mesh for all the nodes in all meshes was 0.8±0.6 mm using the 9 most significant modes of the PCA.

The calculated wall thickness showed that the patients on average had a 13% thicker wall ($p < 0.008$).

IV. DISCUSSION

The developed method provides a framework for decomposing the deformation of an LV FE mesh into several preselected deformation modes between ED and ES. It also quantifies the modes by calculating their corresponding mode coefficients. The 9 chosen modes are reasonably independent as their correlation matrix shows little coupling between the modes. The highest value is between the longitudinal shortening mode, which moves all nodes toward the apex, and the tilting mode, which moves most nodes toward the apex except the ones at the middle of the septum. The wall thickening and hinge mode had the second highest correlation. They both move the endocardial wall inwards but the difference is that

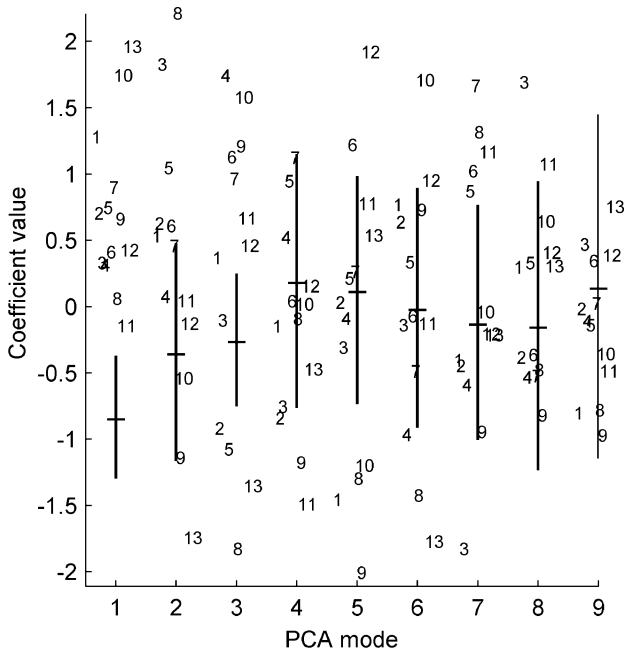

Fig. 4. The figure shows the mean coefficient value for each PCA mode for the normal subjects marked with a short horizontal bar while the vertical line shows the ±SD variation. The coefficients for the patients are indicated with a number for each patient. Their horizontal spread from the mode line is included to separate better between the subjects.

the endocardial nodes are fixed for the wall thickening mode whereas epicardial nodes move inwards by the same amount for the hinge mode. The small degree of mode coupling is further illustrated by the test where the magnitude of one mode was changed one at the time and virtually no other mode coefficient changed value. The modes seem also to capture the total deformation well as is seen by the small error between nodes of the approximated ES mesh with the true ES mesh. The mean error of was 1.7±0.9 mm is a good approximation when one considers that the error of fitting MR tag data is usually in the range of the pixel size (i.e., 1 mm) [6], [7].

There was a distinct difference in the average coefficient values between the two groups for most of the modes. The patients showed less base-apex movement and wall thickening, whereas they had significantly more twist. There was no marked difference in the hinge mode and LR shear mode. The base-tilting mode was quite small for the normal subjects but had a large variance among the patients, which is probably the reason it showed up among the most significant modes of the PCA. The difference in the mode coefficient for the tilting mode for the two groups were close to being statistically significant, and adding more patients to the analysis may make it significantly different. The mean coefficient for the bulging of the septum into the LV was small and negative for the normals, i.e., the septum bulged more into the RV, while most of the patients showed clear symptoms of bulging of the septum into the LV. The bulging mode is interesting, as a common effect of heart failure that reduces contractility is a decreased LV ES pressure where the backward failure elevates RV pressure [15] and may cause some bulging of the septum into the LV.

We can only speculate in the causes for the differences between the normals and patients. The patients were much older and likely to have stiffer myocardium, which impairs myocardial function. Their higher wall thickness may have contributed to the larger twist, which corresponds with a study that compared patients with hypertrophic cardiomyopathy with normal subjects and showed a higher degree of longitudinal twist in the patient group [6]. The higher afterload of the patients may also have altered the deformation.

The relative significance of each mode was indicated by removing it from the mode calculations [(4) and (5)] in order to calculate the mesh error. This showed that longitudinal shortening had by far the most influence on the error, followed by the epicardial twist mode and the hinge mode. Note that the epicardial nodes has a longer "lever"-arm as compared to the endocardial nodes and a rotation of the epicardial nodes by the same angle as the endocardial nodes will move the epicardial nodes a greater distance. The significance of the wall thickening mode came further down the list than what one would expect when considering that the first principle strain direction is usually aligned with the radial direction [16]. One reason for the low significance in our results may be that the MR tagged data was limited in the transmural direction with normally only 1–2 tag-planes through the wall. The tag-planes tended to lie in the mid-wall region, whereas the subendocardium usually has the highest degree of wall thickening [17]. This may have underestimated the wall thickening in our measurements. Mode 4, 7, and 9 had the lowest influence on the error. This may indicate that only small rotation of the endocardial base area occurs (which may be due to the removal of the rigid body rotations). The LR-shearing mode may be a relatively insignificant mode as it has little influence on the error which agrees with a generally small coefficient value and there is no significant difference between the two subject groups for this mode. The reason the septum bulging mode has little impact on the mean error of the 290 nodes for each mesh may be that it only affects a small region of nodes at the center of the septum [see Fig. 2(i)]. The large variance of this mode and the difference between the normals and patients still makes it an interesting mode. Another feature of the changes of the mesh error is the difference in the error increase between the normals and patients for mode 1 and 6. Mode 1 is more pronounced among the normals and, thus, removal of this mode causes a larger increase of the error for the normals than the patients, while the opposite seems to be the case for mode 6.

The PCA extracted modes gave a better approximation of the total deformation as seen by the lower distance between the nodes of the approximated ES mesh and the true ES mesh. Almost all the difference between the two subject groups seems to be captured in the first, most significant mode. The other mode coefficients had too large variances in both of the groups to make any difference statistically significant. A simple test to classify a subject into one of these two groups could be to project it onto mode 1 and check the resulting coefficient. A similar investigation could be carried out on a patient group with different type of disease, i.e., extract the PCA modes for this new group of patients together with normal subjects. The first, most significant PCA mode may then capture most of the difference in the deformation pattern between that patient group and normal subjects and may be used for classification. If one mode is shown

to be clinically useful in a certain application, it may be possible to optimize and simplify the image acquisition procedure to most efficiently capture this mode, e.g longitudinal deformation would be captured just with long-axis images tagged perpendicular to the LV long axis.

The selected modes effect the *global* LV deformation except for the bulging mode, which only applies to the septum region. The coefficient values are a measure of how the total deformation is projected onto these mainly global modes. Patients with regional disease and large regional variations in the deformation are likely to get poorer results for the quantification and approximation in (4). The framework of this method provides a mechanism for implementing other and also regional deformation modes. In case of regional disease such as regional ischemia more bulging modes could be included. If these are placed in areas that are typically affected by the most common ischemic sites the calculated mode coefficients could provide some help in localizing and characterizing the affected area.

We conclude that the developed method successfully decomposes and quantifies the deformation into selected deformation modes. The method also seems capable of separating patients from a group of normal subjects.

ACKNOWLEDGMENT

The authors would like to thank Dr. T. Gentles, Dr. C. Occleshaw, Dr. A. M. Dissanayake, Dr. R. Doughty, Prof. G. Cooper, and Dr. J. Baker for the MR datasets used in this study.

REFERENCES

[1] T. Arts, W. C. Hunter, A. Douglas, A. M. M. Muijtjens, and R. S. Reneman, "Description of the deformation of the left ventricle by a kinematic model," *J. Biomech.*, vol. 25, pp. 1119–1127, Oct. 1992.

[2] J. Park, D. Metaxas, A. A. Young, and L. Axel, "Deformable models with parameter functions for cardiac motion analysis from tagged MRI data," *IEEE Trans. Med. Imag.*, vol. 15, pp. 278–289, June 1996.

[3] W. G. O'Dell and A. D. McCulloch, "Imaging three-dimensional cardiac function," *Annu. Rev. Biomed. Eng.*, vol. 2, pp. 431–456, Aug. 2000.

[4] E. R. McVeigh, "MRI of myocardial function: motion tracking techniques," *Magn. Reson. Imag.*, vol. 14, pp. 137–150, 1996.

[5] N. Reichek, "MRI myocardial tagging," *J. Magn. Reson. Imag.*, vol. 10, pp. 609–616, Nov. 1999.

[6] A. A. Young, C. M. Kramer, V. A. Ferrari, L. Axel, and N. Reichek, "Three-dimensional left ventricular deformation in hypertrophic cardiomyopathy," *Circulation*, vol. 90, pp. 854–867, Aug. 1994.

[7] A. A. Young, D. L. Kraitchman, L. Dougherty, and L. Axel, "Tracking and finite element analysis of stripe deformation in magnetic resonance tagging," *IEEE Trans. Med. Imag.*, vol. 14, pp. 413–421, Sept. 1995.

[8] (2003) *Harrison's Online* [Online] Available: http://harrisons.accessmedicine.com/

[9] A. A. Young, B. R. Cowan, C. J. Occleshaw, H. C. Oxenham, and T. L. Gentles, "Temporal evolution of left ventricular strain late after repair of coarctation of the aorta using 3D MR tissue tagging," *J. Cardiovasc. Magn. Reson.*, vol. 4, pp. 233–243, May 2002.

[10] C. Bradley and A. Pullan, "Geometric modeling of the human torso using cubic hermite elements," *Ann. Biomed. Eng.*, vol. 25, pp. 96–111, 1997.

[11] J. W. Fernandez, P. Mithraratne, S. Thrupp, M. H. Tawhai, and P. J. Hunter, "Anatomically based geometric modeling of the musculo-skeletal system and other organs," *Biomech. Model. Mechanobiol.*, vol. 2, pp. 139–155, Mar. 2004.

[12] K. F. Augenstein and A. A. Young, "Finite element modeling for three-dimensional motion reconstruction and analysis," in *Measurement of Cardiac Deformations from MRI: Physical and Mathematical Models*, A. A. Amini and J. L. Prince, Eds. Dordrecht, The Netherlands: Kluwer Academic, 2001, pp. 37–58.

[13] M. Stuber, M. B. Scheidegger, S. E. Fischer, E. Nagel, F. Steinemann, O. M. Hess, and P. Boesiger, "Alterations in the local myocardial motion pattern in patients suffering from pressure overload due to aortic stenosis," *Circulation*, vol. 100, pp. 361–368, Jul. 1999.

[14] W. H. Press, S. A. Teukolsky, W. T. Vetterling, and B. P. Flannery, *Numerical Recipes in Fortran—The Art of Scientific Computing*, 2nd ed. Victoria, Australia: Cambridge Univ. Press, 1992, p. 667.

[15] A. M. Katz, *Heart Failure—Pathophysiology, Molecular Biology, and Clinical Management*. Philadelphia, PA: Lippincott Williams & Wilkins, 2000, ch. 2.

[16] C. C. Moore, C. H. Lugo-Olivieri, E. R. McVeigh, and E. A. Zerhouni, "Three-dimensional systolic strain patterns in the normal human left ventricle: characterization with tagged MR imaging," *Radiology*, vol. 214, pp. 453–466, Feb. 2000.

[17] K. D. Costa, Y. Takayama, A. D. McCulloch, and J. W. Covell, "Laminar fiber architecture and three-dimensional systolic mechanics in canine ventricular myocardium," *Amer. J. Physiol*, vol. 276, pp. H595–H607, Feb. 1999.

Espen W. Remme was born in Skien, Norway, in 1971. He received the B.Sc. degree in electrical engineering from Telemark Institute of Technology, Porsgrunn, Norway, in 1994 and the M.Sc. degree in engineering cybernetics from the Norwegian University of Science and Technology (NTNU), Trondheim, Norway, in 1998. He received the Ph.D. degree in June 2004 from the same university.

During his Ph.D. work at the Department of Circulation and Medical Imaging at NTNU, he received an overseas fellowship from the Norwegian Research Council to the Bioengineering Institute, University of Auckland, Auckland, New Zealand, where he was a part of the group working there for 3 years. He joined the Institute for Surgical Research, Rikshospitalet University Hospital, Oslo, Norway, in June 2004. His research interests include modeling and simulations of cardiac mechanics and cardiac imaging.

Alistair A. Young was born in Hamilton, New Zealand, in 1962. He received the B.E. degree in engineering science in 1984, the M.E. degree in 1986, and the Ph.D. degree in cardiac image analysis in 1990, all from the University of Auckland, Auckland, New Zealand.

His postdoctoral work at the University of Pennsylvania, Philadelphia, from 1991 to 1993 with Prof. L. Axel involved the analysis of cardiac magnetic resonance images. He is currently Senior Lecturer in Biomedical Imaging at the University of Auckland. His current research interests include cardiac mechanics and biomedical image analysis.

Dr. Young is a member of the International Society of Magnetic Resonance in Medicine, and a founding member of the Society of Cardiovascular Magnetic Resonance.

Kevin F. Augenstein was born in Auckland, New Zealand, in 1977. He received the B.E. (Honors 1st class) degree in engineering science from the University of Auckland, Auckland, New Zealand, in 1999. He is currently working towards the Ph.D. degree at the Bioengineering Institute, University of Auckland, Auckland, New Zealand.

He received a scholarship from the Foundation of Research Science and Technology (New Zealand) to research the use of mathematical models in the analysis of cardiac MRI. His research interests include numerical techniques, mathematical modeling, cardiac mechanics, and imaging.

Brett Cowan was born in Rotorua, New Zealand. He received a first class honors degree in mechanical engineering in 1983 before completing a full medical training in 1993 from the University of Auckland, Auckland, New Zealand.

He has worked in the Department of Medicine at the University of Auckland for the last 6 years performing international clinical trials with MRI to investigate new pharmaceutical agents in the treatment of heart disease. In conjunction with Siemens Medical Systems he works as a biomedical engineer in the postprocessing analysis of cardiovascular MRI images. His clinical interest is in Emergency Medicine and he works as a senior medical officer at North Shore Hospital in Auckland. His current university position is Acting Director of MRI.

Dr. Cowan is a founding member of the Society for Cardiovascular Magnetic Resonance (SCMR), a member of the International Society for MRI Research in Medicine (ISMRM), and a member of the New Zealand Institute of Directors (IOD).

Peter J. Hunter was born in New Zealand. He received the B.E. degree in theoretical and applied mechanics from University of Auckland, in 1971 and the Ph.D. degree in physiology from Oxford University, Oxford, U.K., in 1975.

After a joint postdoc between the Rutherford laboratory and the Engineering Science Department at Oxford he returned to New Zealand in 1980 to found the Bioengineering research group with Prof. Bruce Smaill. He is now the Director of the Bioengineering Institute at the University of Auckland and co-Chair with Prof. Popel of the Physiome and Bioengineering Committee of the International Union of Physiological Sciences (IUPS). He is a member of the IEEE-EMBS Adcom committee.